

A new large-eddy simulation model for simulating air flow and warm clouds above highly complex terrain. Part I: The dry model

Daniel Reinert · Volkmar Wirth · Joachim Eichhorn ·
Walter-Georg Panhans

Received: 12 June 2006 / Accepted: 9 March 2007 / Published online: 11 May 2007
© Springer Science+Business Media B.V. 2007

Abstract This paper presents the dry version of a new large-eddy simulation (LES) model, which is designed to simulate air flow and clouds above highly complex terrain. The model is three-dimensional and nonhydrostatic, and the governing equations are sound filtered by use of the anelastic approximation. A fractional step method is applied to solve the equations on a staggered Cartesian grid. Arbitrarily steep and complex orography can be accounted for through the method of viscous topography. The dynamical model core is validated by comparing the results for a spreading density current against a benchmark solution. The model accuracy is further assessed through the simulation of turbulent flow across a quasi two-dimensional ridge. The results are compared with wind-tunnel data. The method of viscous topography is not restricted to moderately sloped terrain. Compared to models using curvilinear grids, it allows this model to be applied to a much wider range of flows. This is illustrated through the simulation of an atmospheric boundary-layer flow over a surface mounted cube. The results show that the dry model version is able to accurately represent the complex flow in the vicinity of three-dimensional obstacles. It is concluded that the method of viscous topography was successfully implemented into a micrometeorological LES model. As will be shown in Part II, this allows the detailed study of clouds in highly complex terrain.

Keywords Complex orography · Inflow turbulence · Large-eddy simulation · Turbulent flow

1 Introduction

In the last 10 years the technique of large-eddy simulation (LES) has gained more and more attention because of the continuously increasing computer capacity. Large-eddy simulations can be regarded as an approach intermediate between direct numerical simulations (DNS) and

D. Reinert (✉) · V. Wirth · J. Eichhorn · W.-G. Panhans
Institute for Atmospheric Physics, Johannes Gutenberg-University Mainz, Becherweg 21, 55099 Mainz,
Germany
e-mail: dreinert@uni-mainz.de

methods based on the Reynolds averaged Navier Stokes equations (RANS). For a detailed introduction into the LES technique and its distinction from DNS see [Froehlich and Rodi \(2001\)](#).

In the case of DNS, the turbulent fluctuations of all scales are simulated explicitly and no turbulence closure is needed. For this to be successful, the mesh spacing has to be smaller than the smallest emerging scales of motion. As the smallest length scales of the flow decrease very rapidly with increasing Reynolds number, current DNS are limited to Reynolds numbers of the order $Re \sim 10^3$ ([Neumann and Wengle 2003](#)). Even in the next few decades the application of DNS to geophysical flows ($Re > 10^5$) seems unlikely.

RANS models are much less computer time consuming, since only the mean flow is simulated explicitly while the effects of all turbulent fluctuations are parameterised by a turbulence closure model. Although very efficient, this method gives inaccurate results when applied to complex flow with boundary-layer separation because of the basic assumptions underlying RANS models. Especially the need for the parameterisation of larger scale turbulent eddies leads to major uncertainties and errors, since their overall character is strongly problem dependent.

The latter problem is overcome in large-eddy simulations. The main idea is to simulate the larger and most energy containing scales of the flow explicitly and to parameterise only the effect of the smaller subgrid-scale turbulence, using a so-called subgrid-scale (SGS) model. If the mesh spacing lies in the inertial subrange of three-dimensional turbulence, most of the energy containing eddies and the mechanisms of energy production will be simulated explicitly. The main physical role of the SGS eddies then is to dissipate the energy, which cascades down from the larger (explicitly simulated) scales. Therefore, the basic requirement of an SGS model is to provide energy dissipation at the correct dissipation rate. One major advantage of LES compared to the RANS technique is that the remaining subgrid-scale turbulence tends to be more universal, with eddies that are relatively invariant in character between different parts of the flow and between different flows. There is some evidence that a successful closure is more likely to be achieved by LES, even with relatively simple SGS models, than by the RANS method.

In the meteorological community LES models have been extensively and successfully used to simulate planetary boundary-layer turbulence assuming plane and infinite lower boundaries. A pioneering work is the boundary-layer simulation of [Deardorff \(1972\)](#). Another example is the detailed study of the convective planetary boundary layer by [Mason \(1989\)](#).

Few LES models exist in the meteorological literature which include both moist thermodynamics and irregular lower boundaries. Moreover, few models apply more realistic open inflow/outflow boundaries instead of highly idealised periodic boundaries. For example, the models presented by [Allen and Brown \(2002\)](#) and [Kanda et al. \(2004\)](#) are able to account for irregular lower boundaries, but they are restricted to periodic boundary conditions. This evades the problem of providing reasonable turbulent inflow data. [Iizuka and Kondo \(2006\)](#) present simulations of air flow over moderately sloped terrain using a comprehensive inflow generation technique, but their model, as well as the others mentioned, does not include moist thermodynamics.

The main objective of our work is the simulation of air flow and clouds over non-periodic complex orography. Only few current LES models are suitable to perform this work. Possibly this is related to the difficulties associated with the simulation of wall-bounded shear flows, the implementation of a complex lower boundary, and the necessity of more complicated open inflow and outflow conditions.

As the first part of a two-part series we describe herein the dry dynamics of our new LES model, focussing on the simulation of air flow in the vicinity of complex orography. In part II

we will present and validate a two-moment microphysical bulk scheme which provides the possibility to simulate and investigate clouds in general, and orographically induced clouds in particular.

In the next section, the governing model equations and their numerical treatment will be presented in some detail. Sections 3 and 4 present results of different model tests. Finally, some conclusions will be given in Sect. 5.

2 Model description

Our LES model is three-dimensional and nonhydrostatic. The anelastic approximation is applied to filter out sound waves, which enables a much larger timestep for time integration. This implies that an elliptical equation for the pressure has to be solved at every timestep. The governing equations are discretised with finite differences on a staggered Cartesian Arakawa-C grid, permitting the treatment of arbitrarily steep orography.

2.1 Model equations

The prognostic variables of the dry model are the three velocity components u , v , w , for the x -, y -, and z -directions, respectively, the potential temperature θ , and the nonhydrostatic pressure perturbation p' . The equations of motion for the resolved scales can formally be derived by applying a filtering operation to the governing equations. In combination with the anelastic approximation the filtered Navier–Stokes equations take the following form:

$$\frac{\partial}{\partial x_i}(\rho_0 \bar{u}_i) = 0 \tag{1}$$

$$\rho_0 \frac{\partial \bar{u}_i}{\partial t} + \frac{\partial}{\partial x_j}(\rho_0 \bar{u}_j \bar{u}_i) = -\frac{\partial p'}{\partial x_i} + \rho_0 g \frac{\theta'}{\theta_R} \delta_{i3} + \frac{\partial}{\partial x_j} \tau_{ij}^{SGS}. \tag{2}$$

In this case the Coriolis term has been omitted. The effect of the unresolved scales appears through the SGS stress term $\tau_{ij}^{SGS} = -\rho_0 (\overline{u_i u_j} - \bar{u}_i \bar{u}_j)$, which has to be modelled. The filtered heat equation in terms of potential temperature for an anelastic fluid can be written as

$$\frac{\partial \bar{\theta}}{\partial t} + \frac{1}{\rho_0} \frac{\partial}{\partial x_i}(\rho_0 \bar{u}_i \bar{\theta}) = \frac{1}{\rho_0 c_{p0}} \left(\frac{p_{00}}{p_0} \right)^{\frac{R_d}{c_{p0}}} \left(\bar{Q}^h - \frac{\partial}{\partial x_i} F_i^h \right). \tag{3}$$

In the above, the Einstein summation notation is used, \bar{u}_i represents the filtered velocity components, g is the gravitational acceleration, ρ_0 and p_0 are the vertically variable but time independent density and hydrostatic pressure, respectively, $p_{00} = 1,013$ hPa is a constant reference pressure, R_d is the gas constant for dry air, c_{p0} is the heat capacity for dry air at constant pressure, \bar{Q}^h denotes sources of diabatic heating (like the release of latent heat), θ_R is the potential temperature of a reference state (initial profile) and the prime denotes deviations from corresponding reference values.

For notational simplicity the overbar, denoting the filtered quantities, will be dropped from now on.

2.1.1 The SGS model

The unknown SGS momentum fluxes τ_{ij}^{SGS} and heat fluxes F_i^h have to be parameterised with the aid of a subgrid-scale model. We apply the widely used Lilly-Smagorinsky SGS model

(Lilly 1962). It is an algebraic model based on the assumption of local balance between production and dissipation of SGS turbulent energy.

Since the subgrid stress τ_{ij}^{SGS} is not strictly deviatoric it will be split into an isotropic part τ^I and a deviatoric part τ_{ij}^D :

$$\tau_{ij}^{SGS} = \tau^I \delta_{ij} + \tau_{ij}^D \tag{4}$$

with

$$\tau_{ij}^D = \tau_{ij}^{SGS} - \frac{1}{3} \tau_{kk}^{SGS} \delta_{ij}. \tag{5}$$

The deviatoric part τ_{ij}^D is related to the resolved shear stress by

$$\tau_{ij}^D = 2\rho_0 K_m \left(S_{ij} - \frac{1}{3} S_{kk} \delta_{ij} \right), \tag{6}$$

with the exchange coefficient K_m for momentum and the strain rate of the resolved velocity field

$$S_{ij} = \frac{1}{2} \left(\frac{\partial u_i}{\partial x_j} + \frac{\partial u_j}{\partial x_i} \right). \tag{7}$$

Since the isotropic part of the SGS stresses τ^I is indistinguishable from pressure it is assumed to be included into the resolved pressure perturbation p' .

Dimensional analysis suggests the exchange coefficient K_m to be a combination of a length scale, representative for the unresolved motions and a resolved velocity scale. With an additional term including buoyancy effects, the Lilly–Smagorinsky model for K_m reads

$$K_m = \begin{cases} (C_s \Delta)^2 |S_{ij}| \sqrt{1 - Ri} & \text{if } Ri < 1 \\ \nu_{\text{air}} & \text{if } Ri \geq 1 \end{cases} \tag{8}$$

with the viscosity of air ν_{air} , the magnitude of the rate of strain tensor

$$|S_{ij}| = (2 S_{ij} S_{ij})^{\frac{1}{2}}, \tag{9}$$

the Richardson number

$$Ri = \frac{g}{\theta} \frac{\partial \theta}{\partial z} \frac{1}{2 S_{ij} S_{ij}}, \tag{10}$$

and the mean grid length $\Delta = (\Delta_x \Delta_y \Delta_z)^{1/3}$. C_s is an empirical constant, also known as the Smagorinsky constant, whose value depends on the type of flow and the numerical schemes applied. Values in the range $0.065 \leq C_s \leq 0.2$ are reported in the literature (see Clark et al. (1979) and Moin and Kim (1982) for the limiting values). Since C_s is real, the Smagorinsky model is absolutely dissipative and, thus, not able to represent backscatter. A possible extension of the Smagorinsky model, which enables backscatter of energy, is described by Mason and Thomson (1992).

Putting it all together, in the case of $Ri < 1$ the parameterisation of the deviatoric SGS stresses reads

$$\tau_{ij}^D = 2\rho_0 l_0^2 |S_{ij}| \sqrt{1 - Ri} \left(S_{ij} - \frac{1}{3} S_{kk} \delta_{ij} \right). \tag{11}$$

Here, the mixing length $l_0 = C_s \Delta$ has been introduced.

For $Ri \geq 1$ the parameterisation of the deviatoric SGS stresses simplifies to

$$\tau_{ij}^D = 2\rho_0 \nu_{\text{air}} \left(S_{ij} - \frac{1}{3} S_{kk} \delta_{ij} \right). \tag{12}$$

The unresolved heat fluxes F_i^h are determined similarly to τ_{ij}^D with a flux–gradient relationship

$$F_i^h = -\rho_0 c_{p0} K_h \frac{\partial \theta}{\partial x_i}. \tag{13}$$

The exchange coefficient K_h for heat is calculated based on the exchange coefficient for momentum by setting $K_h = 1.35 K_m$, which is strictly valid only for neutral conditions.

2.2 Solution strategy

During the numerical time integration, the heat equation (3) is solved first to provide an updated buoyancy term for the momentum equation. This is done in two steps: in a first substep we compute the tendency due to the advection, and in a second substep we compute the tendencies due to the SGS fluxes and the sources/sinks of diabatic heating. Afterwards, Eqs. 1 and 2 are solved via the so-called fractional step or projection method. Here we follow the work of [Patrinos and Kistler \(1977\)](#). First, the momentum equation is solved by neglecting the pressure gradient, and an auxiliary velocity field \tilde{u}_i is obtained. This is, again, done in two steps, where in a first substep the advection part is dealt with, and in a second substep the diffusion part is solved with the added buoyancy term.

The auxiliary velocity field does not necessarily satisfy the incompressibility constraint imposed by the continuity equation. To enforce the divergence constraint (1), a Poisson equation for the pressure perturbation p' has to be solved. Between the updated auxiliary velocity \tilde{u}_i^{n+1} and the real velocity u_i^{n+1} the following relationship exists:

$$\rho_0 \tilde{u}_i^{n+1} = \rho_0 u_i^{n+1} + \Delta t \frac{\partial p'^{n+1}}{\partial x_i}. \tag{14}$$

Taking the divergence of this equation and considering the continuity equation (1) leads to an elliptic equation, which combines the pressure perturbation and the auxiliary wind field \tilde{u}_i :

$$\nabla^2 p'^{n+1} = \frac{1}{\Delta t} \frac{\partial \left(\rho_0 \tilde{u}_i^{n+1} \right)}{\partial x_i}. \tag{15}$$

The solution of this equation gives a new pressure perturbation field, which can then be used to compute the new velocity field by solving (14) for u_i^{n+1} .

2.3 Numerical methods

Different numerical methods are used for different parts of the governing equations.

Advection is performed with two different explicit numerical schemes, which are both of second-order accuracy in time and space. For the advection of momentum the MacCormack scheme ([MacCormack 1969](#)) is applied, which is a Lax-Wendroff type finite difference technique widely used in aerospace simulations. This scheme is characterised by very low phase speed errors ([Mendez-Nunez and Caroll 1993](#)), but it is non-monotonous like all higher order schemes that do not use a flux correction. In the case of linear advection the Lax-Wendroff scheme and the MacCormack scheme are essentially equal. In the nonlinear case

the MacCormack scheme is preferable to the Lax-Wendroff scheme because it is simpler to implement. It is a predictor corrector scheme with an upstream discretisation in the predictor and a downstream discretisation in the corrector step, or vice versa. To enhance the stability of the scheme the discretisation of the predictor and corrector are cyclically changed from upstream to downstream at every timestep, as recommended by MacCormack (1969).

The only scalar quantity that has to be advected in the dry model version is the potential temperature θ . For this we apply the MPDATA scheme of Smolarkiewicz and Clark (1986). In order to avoid nonphysical over- and under-shoots in advected fields exhibiting a non-zero background value (e.g. potential temperature and specific humidity) the scheme has been expanded to a monotonous one (Smolarkiewicz and Grabowski 1990).

The SGS turbulent fluxes of heat and momentum are handled implicitly by the alternating direction implicit (ADI)-method of Douglas (1962), which is second order in space and time.

The discrete form of the elliptical pressure equation (15) is solved iteratively with the idealised generalised conjugate gradient (IGCG)-method as described by Kapitza and Eppel (1986). To account for grid cells that are intersected by orography, the discretised pressure equation has been expanded by so-called ‘cell boundary weight factors’. For more information regarding the solution of the Poisson equation and the inclusion of ‘cell boundary weight factors’ the reader is referred to the documentation of our related mesoscale model CliMM (Eichhorn et al. 1997).

2.4 Treatment of orography

The model uses a Cartesian grid and is, therefore, in principle capable of handling arbitrarily steep orography. To improve the crude steplike boundary representation that is typical for Cartesian models, we use the method of viscous topography first suggested by Mason and Sykes (1978). For ease of reference this method will be briefly outlined here.

Air and orography are treated as two fluids with vastly different viscosities. Due to this artifice, the governing equations, and especially the Poisson equation for pressure, can be solved on the entire rectangular domain without regard to the position of the orography. If the viscosities were set to K_m in the air and infinity in the orography, this would result in a steplike approximation of the orography. To improve on this, the viscous stress term is modified near the lower boundary. More specifically, the viscous stresses are made continuous through the boundary by calculating a so-called ‘interpolated viscosity’ at the interface between air and orography. This interpolated viscosity accounts for the intersection of the grid cells by orography.

The method is applied in three dimensions, and will be explained here for the viscous stress component $\tau_{13} = \rho_0 K_m \frac{\partial u}{\partial z}$. Figure 1 considers the u -velocity component along a vertical line through several grid cells. The orography S intersects a grid cell at point R . The definition points of u are symbolised by dots, and due to the staggering the exchange coefficients K_m are defined at intermediate points denoted by \times . Below the surface S the points are assumed to be inside of the orography, while the points above S belong to the atmosphere. The viscosity of the orography is denoted by ν_s . Inside the atmosphere the time dependent exchange coefficient K_m is used which is provided by the SGS model. Whenever a viscous stress term has to be calculated involving velocity values from both sides of the surface S , we refer to the layer inbetween as an interpolation layer and use the interpolated viscosity ν_{int} (point M in Fig. 1). The thickness of the interpolation layer is denoted by Δ and the distance of the lower u -velocity component from the surface is ϵ .

The requirement of continuous stresses across the surface is equivalent to the assumption of constant stresses inside the interpolation layer. We can thus approximate the shear stress in the following different ways:

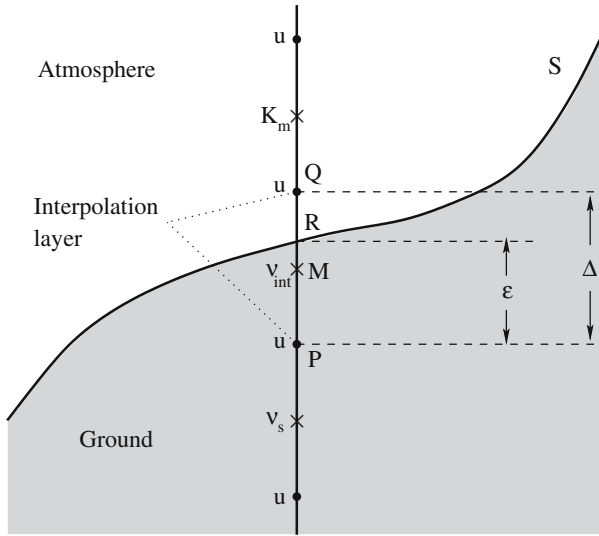


Fig. 1 Illustrating the derivation of the interpolated viscosity v_{int} for calculating the stress $\rho_0 v \frac{\partial u}{\partial z}$

$$\tau_{13} \approx \rho_0 K_m \frac{u_Q - u_R}{\Delta - \epsilon} = \rho_0 v_s \frac{u_R - u_P}{\epsilon}. \tag{16}$$

From this equation u_R can be eliminated and we obtain

$$\tau_{13} = \frac{\rho_0 K_m v_s (u_Q - u_P)}{K_m \epsilon + v_s (\Delta - \epsilon)}. \tag{17}$$

When this is compared to the result of the model discretisation

$$\tau_{13} = \rho_0 v_{int} \frac{u_Q - u_P}{\Delta}, \tag{18}$$

this leads to the required interpolated viscosity

$$v_{int} = \frac{K_m v_s \Delta}{K_m \epsilon + v_s (\Delta - \epsilon)}. \tag{19}$$

We avoid the limit $v_s \rightarrow \infty$ because of numerical problems that arise if $\Delta = \epsilon$. Instead we use the approximation

$$v_{int} = K_m \frac{v_s \Delta}{c \epsilon + v_s (\Delta - \epsilon)} \tag{20}$$

with a constant exchange coefficient c providing the correct order of magnitude and $v_s = 10^{16} \text{ m}^2 \text{ s}^{-1}$. It is a valid approximation as long as $K_m/v_s \ll \Delta/\epsilon - 1$ which is almost always the case. Equation 20 is favourable over (19) since the second factor in (20) needs to be calculated only once. It can be used as a constant correction factor for the exchange coefficient K_m at the first grid point outside of the orography.

2.5 Boundary conditions

2.5.1 The physical lower boundary

The occurrence of the lower solid boundary inside the model domain requires special care. If solid boundaries are present, the size of the energy containing eddies scales approximately with the distance from the wall. In order to account for the most important structures the grid would have to be enormously refined near the wall. This would almost result in a DNS near the wall, which is not feasible for high Reynolds number flows. A much coarser resolution can be applied by bridging the region very close to the wall with the help of a wall function (see Cabot and Moin (1999) for a review). A wall function provides a relationship between the local wall shear stress and the velocity at the first interior grid point. Although this method is known to provide only crude approximations of the real wall shear stresses, especially in regions of flow separation, it gives fair results and is widely used.

An estimate of the wall shear stress τ_w at every timestep can be obtained by assuming a functional relationship between the velocity component u_{\parallel} parallel to the wall at the first interior grid point (with a distance η perpendicular to the wall) and the shear stress τ_w .

In the surface layer τ_w is related to the friction velocity u_* by $\tau_w = \rho_0 u_*^2$. If it is further assumed that the velocity profile between the first interior grid point and the wall with surface roughness z_0 obeys a logarithmic law, the instantaneous value of τ_w can be calculated as

$$\tau_w = \rho_0 \frac{\kappa^2 u_{\parallel}^2}{\ln\left(\frac{\eta}{z_0}\right)^2}, \quad (21)$$

where κ is the von Kármán constant.

The numerics of our LES model do not foresee the application of a wall shear stress as lower boundary condition. Instead an approximation for the first interior exchange coefficient has to be derived, which can then be used as input for our numerical scheme. For this purpose the wall shear stress is expressed in an alternative manner by assuming the flux–gradient relationship

$$\tau_w = \rho_0 K_m \frac{\partial u_{\parallel}}{\partial n}, \quad (22)$$

with n denoting the direction perpendicular to the wall. If u_{\parallel} is again approximated by the logarithmic profile, τ_w can be eliminated by equating (21) and (22). This results in an expression for the first interior exchange coefficient K_m :

$$K_m = \frac{\kappa^2 u_{\parallel} \eta}{\ln\left(\frac{\eta}{z_0}\right)}. \quad (23)$$

In addition to applying a wall model for the nearest grid point, the Smagorinsky SGS model is modified, too, in order to account for the fact that near solid walls the subgrid turbulent stresses vanish. In the viscous sublayer, next to the wall, the viscous forces dominate and the turbulent contribution to the shear stress vanishes since the velocities $u_i \rightarrow 0$ as the wall is approached.

An appropriate asymptotic behaviour of the SGS model can be achieved by using a different mixing length l in the vicinity of the wall and a smooth blending between the near wall value and the value in the inner flow l_0 . We use a blending that was suggested

by Mason (1994), and we substitute the mixing length l_0 in (11) by l , which is defined as

$$\frac{1}{l^2} = \frac{1}{[\kappa(\eta + z_0)]^2} + \frac{1}{l_0^2}, \quad (24)$$

where η denotes, again, the distance perpendicular to the wall. Near the wall the mixing length l equals the Prandtl mixing length.

2.5.2 Boundary conditions at artificial boundaries

At the upper boundary a rigid lid is implemented using a free slip condition for the horizontal velocity components ($\frac{\partial(u, \tilde{u})}{\partial z}|_{\text{top}} = \frac{\partial(v, \tilde{v})}{\partial z}|_{\text{top}} = 0$) and a Dirichlet condition for the vertical velocity ($w|_{\text{top}} = 0$). At the lateral boundaries various conditions are possible depending on the problem under consideration. Closed and periodic boundaries can be used as well as open inflow/outflow boundaries.

Inflow boundaries using time dependent Dirichlet conditions are non-trivial, since the inflow already must comprise reasonable turbulent structures. We implemented an inflow generation technique similar to the one described in Kataoka and Mizuno (2002). It is a simplified version of the perturbation recycling method proposed by Lund et al. (1998) assuming a constant boundary-layer thickness. More details can be found in Sect. 4.

At open outflow boundaries we require a no flux condition for the tangential velocity components u_i , \tilde{u}_i and for all scalar variables. For the normal components of the auxiliary wind field \tilde{u}_i either no flux conditions or radiation boundary conditions (Orlanski 1976) can be used. We found the no flux condition to be reasonable in most cases, additionally leading to a slightly improved convergence of the pressure solver.

At inflow boundaries we additionally require a no flux condition for the pressure of the form $\frac{\partial p'}{\partial n}|_{\text{inflow}} = 0$. This implies $u_i = \tilde{u}_i$ for the velocity component normal to the boundary.

At the outflow boundaries the pressure is corrected in order to achieve conservation of the total mass in the model domain. Whether the outflow or inflow condition for the pressure should be used is decided independently for every grid cell at every timestep. For a detailed description of this procedure the reader is referred to Eichhorn et al. (1997).

3 Validation of dynamical model core

The following simulation of an idealised density current presents an important test to confirm the reliability of the dynamical model core.

In this test a two-dimensional cold bubble (x - z -plane) is initiated at a given height above the lower boundary. It descends to the ground, spreads out laterally and rotors form at the top of the spreading cold pool due to Kelvin–Helmholtz instabilities.

Our model set-up follows the work of Straka et al. (1993), who provides a benchmark solution for comparison. The SGS model is switched off and a constant viscosity of $75 \text{ m}^2 \text{ s}^{-1}$ is used for the momentum and potential temperature fields. Thus the resolvable scales are limited by the prescribed eddy viscosity and not by the grid size. We apply a free slip condition at the lower boundary and a rigid lid condition at the upper boundary. At the lateral boundaries periodical boundary conditions are used.

The model domain has a horizontal extent of 51.2 km and a vertical extent of 6.4 km. At the beginning of the simulation, the atmosphere is at rest ($u = w = 0 \text{ m s}^{-1}$), horizontally homogeneous, hydrostatically balanced, and neutrally stratified with a constant potential

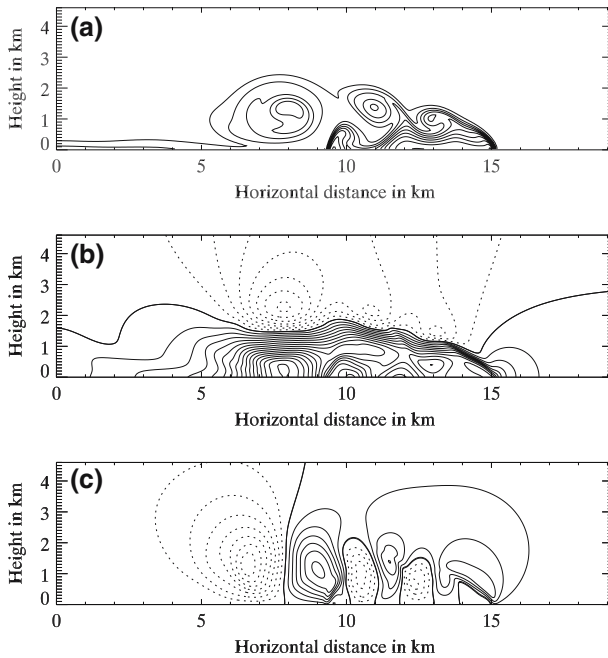


Fig. 2 Contour plot of the density current after 15 min with a resolution of 50 m. Only the right portion of the domain is shown. (a) θ' , (b) u , (c) w . Contour intervals (a) 1 K, (b) 2 m s^{-1} , (c) 2 m s^{-1} . All contours are centred around the zero line

temperature of $\theta = 300 \text{ K}$. To initiate the density current, a bubble shaped temperature disturbance is implemented at the centre of the model domain with a maximum temperature anomaly of -15 K . The shape of the temperature disturbance ΔT in kelvin is given by

$$\Delta T = \begin{cases} -15.0 \cos^2\left(\frac{\pi}{2} L\right) & \text{if } L \leq 1 \\ 0.0 & \text{if } L > 1 \end{cases} \quad (25)$$

with

$$L = \left(\left(\frac{x - x_c}{x_r} \right)^2 + \left(\frac{z - z_c}{z_r} \right)^2 \right)^{\frac{1}{2}}. \quad (26)$$

The subscripts ‘c’ and ‘r’ refer to the centre position and radial extent of the bubble. For $x_c, z_c, x_r,$ and z_r we choose the values 0, 3, 4, and 2 km, respectively. For further details regarding the model set-up see [Straka et al. \(1993\)](#).

Two model runs have been carried out, one with a grid spacing of $\Delta x = \Delta z = 100 \text{ m}$ and one with $\Delta x = \Delta z = 50 \text{ m}$. Figure 2 shows the simulated potential temperature anomaly θ' and the velocity components u, w at $t = 15 \text{ min}$ for the 50 – m resolution case.

The results agree well with the 25 m grid converged reference solution given by [Straka et al. \(1993\)](#). After 15 min three rotors have formed along the top of the cold air due to the Kelvin–Helmholtz instability, as can be seen in Fig. 2a. Even in the 100 – m grid simulation the overall behaviour and the three rotors are well captured (see Fig. 3).

In Table 1 the maximum and minimum values of u, w, θ', p' and the front location of the current at $t = 15 \text{ min}$ are listed. The values are compared to the results of the quasi

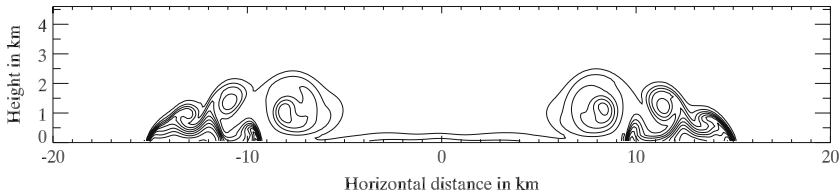


Fig. 3 Isolines of the potential temperature anomaly θ' for the translating density current after $t = 15$ min on a 100 m grid. Differences in the left and right moving current indicate phase errors. The translation velocity is $u_{trans} = 20 \text{ m s}^{-1}$. The contour interval is 1 K and the contours are centred around the zero line

Table 1 Maximum and minimum values of u, w, θ', p' and the front location of the density current at 15 min for the quasi compressible reference model of Straka et al. (1993) (REFQ25) and our LES model with 50 – m resolution (LES50) and 100 – m resolution (LES100)

	REFQ25	LES50	LES100
Front location (m)	15509	15190	15200
u_{max} (m s^{-1})	34.72	32.35	30.49
u_{min} (m s^{-1})	-15.31	-14.31	-13.64
w_{max} (m s^{-1})	13.04	12.47	12.15
w_{min} (m s^{-1})	-16.89	-15.26	-15.07
θ'_{max} (K)	0.00	0.00	0.01
θ'_{min} (K)	-10.00	-9.77	-10.40
p'_{max} (hPa)	1.74	1.27	1.43
p'_{min} (hPa)	-5.21	-4.88	-4.29

compressible reference model of Straka et al. (1993). It can be seen that the results of the 50 – m resolution run agree fairly well with the 25 m benchmark solution of Straka et al. (1993). In our simulations the front location of the density current seems to be slightly underestimated. The same holds for the velocity maxima and minima. Whereas the simulated front location seems to be fairly unaffected by the grid resolution, the underestimation of the velocity maxima and minima decreases significantly with increasing resolution. Thus, at least the results for the velocity maxima and minima seem to converge to those of the reference solution with increasing resolution.

On the 100 m grid this test case has been repeated with a constant translation velocity of 20 m s^{-1} added to the initial conditions. The occurring discrepancies between the left and right moving density current give an indication of the phase errors for the combination of the MacCormack scheme and MPDATA. Figure 3 shows both parts of the density current in terms of θ' after $t = 15$ min. As can be seen, the differences between the right and left moving current are small even on the 100 m grid. This indicates that the dynamical model core does not suffer from large phase errors, which could significantly degrade the simulation.

4 LES of flow over complex terrain

The following section presents two LES of fully turbulent flow over irregular terrain using non-periodic inflow/outflow boundary conditions. As two relevant test cases we chose the

flow of a turbulent boundary layer over a quasi 2D ridge and a 3D cube. Although the topography is quite simple in both cases, the associated flow field is highly complex, since features like flow separation, reattachment and recirculation occur. Moreover, in the case of a 3D cube, periodical vortex shedding is known to exist in the lee. These test cases have been selected for two reasons: first, they are well suited for model validation, since experimental as well as numerical investigations have already been reported in the literature. Second, these set-ups present a critical test for the method of viscous topography and especially the inflow generation technique mentioned in Sect. 2.5.2. The generation of fully turbulent inflow data that satisfy given statistical properties is a prerequisite for a successful LES in an open domain.

4.1 Flow over two-dimensional ridge

The model is used to simulate the turbulent flow over an aerodynamically rough two-dimensional ridge in a neutrally stratified environment. The Reynolds number based on the free stream velocity, the hill height and v_{air} is $Re = 1.58 \times 10^4$. The accuracy of these computations will be assessed by comparing the results with those from a wind-tunnel experiment by Ishihara et al. (2001). Our model set-up is similar to that described by Iizuka and Kondo (2006) who also tried to reproduce the wind-tunnel data numerically. Their results will also be referenced where appropriate.

4.1.1 Model set-up and inflow generation

The geometry of the computational domain is shown in Fig. 4, where distances are given as a multiple of the hill height $H = 40$ mm. Open boundary conditions are used in the x -direction, while periodic boundaries are applied in the y -direction. The computational domain covers $60 H(x) \times 4 H(y) \times 24 H(z)$ using $300 (x) \times 20 (y) \times 48 (z)$ grid cells. We applied a uniform grid spacing of $\Delta x = \Delta y = 0.2 H$ in the streamwise and spanwise directions. In the vertical direction a stretched grid was used starting with the first vertical level at $z = 0.05 H$. The grid stretching ratio was set to a value of 1.05 for $z < 1.2 H$ and was increased to 1.1 above. The Smagorinsky constant was set to $C_s = 0.1$ in this study, which is a generally accepted value for shear driven flows (Iizuka and Kondo 2006). The roughness length was set to $z_0 = 0.0075 H$, as given by Ishihara et al. (2001).

To provide reasonable turbulent inflow data, a precursor computation was performed applying the implemented inflow generation technique. This precursor simulation differed from the main simulation in only three points:

- a modified inflow boundary condition as described by Kataoka and Mizuno (2002)
- homogeneous lower boundary (no hill)
- reduced domain size of $11 H(x) \times 4 H(y) \times 24 H(z)$.

In order to create the turbulent inflow data, the only thing that needs to be specified is the mean velocity profile above the flat lower boundary. This velocity profile was also provided by Ishihara et al. (2001). After the inflow generator reached a statistically steady state, slices of the instantaneous velocity fields were stored on disk for 250 nondimensional time units based on the free stream velocity $U_\infty = 5.9 \text{ m s}^{-1}$ and H . In the following main run this dataset was used at the inflow boundary. Since the main run exceeded the timespan for which inflow data could be stored, the inflow dataset was repeated cyclically. At the outflow boundary a simple zero gradient condition was applied.

Figure 5a, b shows vertical profiles of the time mean velocity $\langle u \rangle$ and standard deviations σ_i for the stored inflow data. The experimental results are shown for comparison. As can be

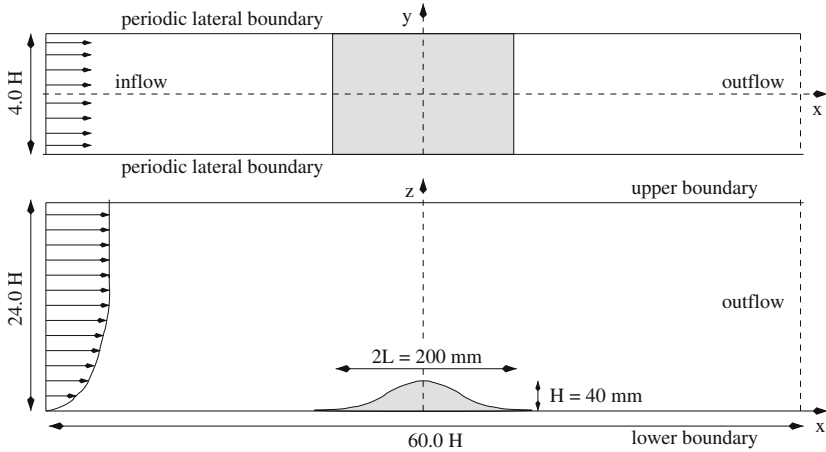


Fig. 4 Geometry of the computational domain for the 2D hill experiment. Distances are given as a multiple of the hill height H . L gives the width of the hill

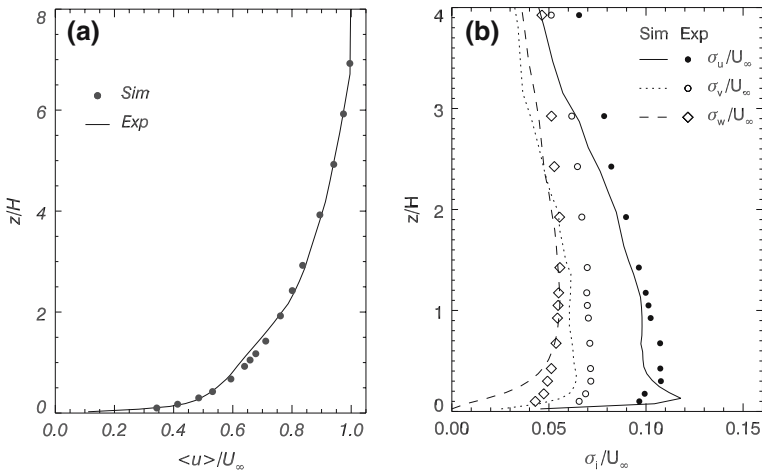


Fig. 5 Characteristics of the generated inflow data. **(a)** Vertical profile of time-averaged streamwise velocity $\langle u \rangle / U_\infty$; **(b)** velocity standard deviations σ_u / U_∞ , σ_v / U_∞ , σ_w / U_∞ for the x -, y -, and z -directions, respectively. Lines indicate model results and symbols indicate experimental data

seen, the mean velocity profile is fairly well reproduced. This confirms the appropriateness of our lower boundary condition at least under horizontal homogeneous conditions (see Sect. 2.5.1). Otherwise strong deviations from the measurements would occur especially near the lower boundary. Similarly, even the turbulent fluctuations agree well with the measurements (Fig. 5b), although no a priori assumption was made about their vertical structure or absolute values.

Fig. 6 Streamlines of simulated time-averaged flow field. Approaching flow from left to right

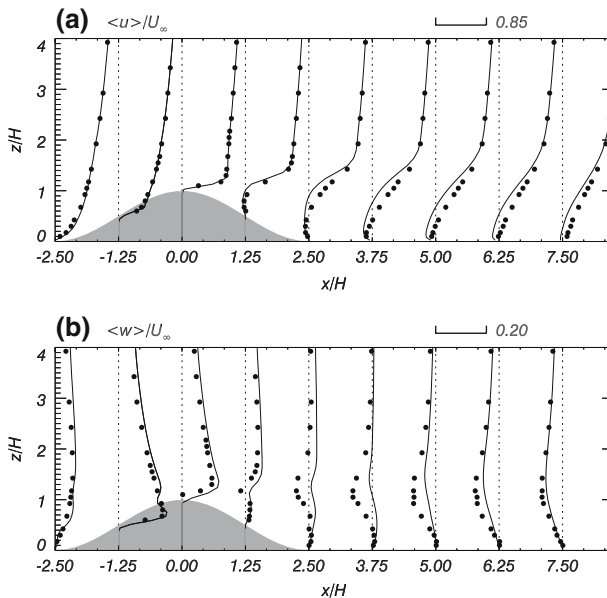
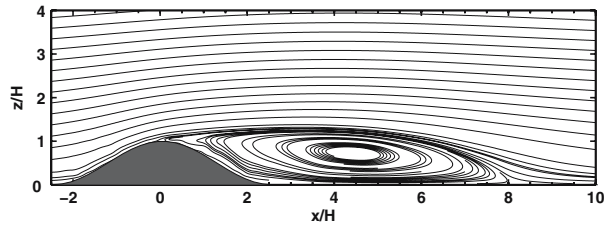


Fig. 7 Vertical profiles of time-averaged velocities. **(a)** streamwise component $\langle u \rangle / U_\infty$, **(b)** vertical component $\langle w \rangle / U_\infty$. Lines indicate model results and filled circles indicate experimental data

4.1.2 Results

The main simulation was run for $\Delta t = 1,000$ nondimensional time units. The time-averaged results shown in Figs. 6, 7 and 8 were determined by averaging over the last 750 nondimensional time units and by averaging in the spanwise (y) direction.

Figure 6 shows streamlines of the simulated mean flow field near the hill. The main characteristics of this flow field are the separation at hill top, the corresponding recirculation region downstream and the acceleration above the hill (which may be seen more clearly in Fig. 7a). The length of the recirculation region is slightly overestimated by our model (reattachment point at $x/H = 8$ compared to $x/H = 6.4$ in the experiment). Nevertheless, the results compare well with the experimental data. This is confirmed by Fig. 7a, b which shows vertical profiles of the streamwise and vertical velocity at various points near the hill. For comparison experimental results are included. As can be seen, our results fit very well up to approximately $x/H = 1.25$. The differences further downstream are mainly a result of the overestimated reattachment length.

Figure 8a–c shows vertical profiles of the velocity standard deviations σ_u , σ_v and σ_w at various locations near the hill. Again experimental results are shown for comparison. While

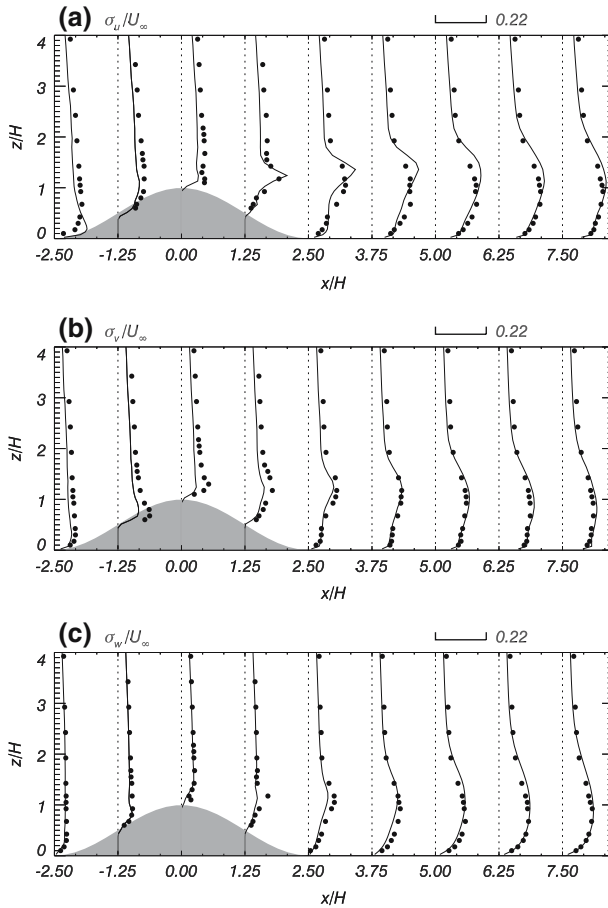


Fig. 8 Vertical profiles of resolved velocity standard deviations. (a) σ_u / U_∞ , (b) σ_v / U_∞ , (c) σ_w / U_∞ . Lines indicate model results and filled circles indicate experimental data

σ_v and σ_w agree well with the experimental results, even in the lee of the hill, σ_u is slightly overestimated along the free shear layer. Nevertheless, this overestimation, which is a well known problem of the Smagorinsky SGS model, is less pronounced than in the simulation of Iizuka and Kondo (2006).

Beside this slight overestimation, an upward bias regarding the maxima for σ_u can be seen. This corresponds to an upward displacement of the separating free shear layer compared to the experimental results. The latter problem is not related to the Smagorinsky SGS model, since Iizuka and Kondo (2006) do not observe this feature when using the Smagorinsky model. We think that it is related to our method of viscous topography. This upward bias may also contribute to the overestimated reattachment length. Other reasons for this may be our numerical methods or the horizontal and vertical resolution. We verified that the reattachment length is only slightly affected by moderate changes in turbulence intensities at the inflow boundary. Thus the small differences between the measured and simulated standard deviations at the inflow boundary (Fig. 5b) cannot account for the overestimated reattachment length.

4.2 Flow around a surface mounted cube

The second test case highlights the fact that our model domain is not restricted to moderately sloped terrain as is the case for many models using curvilinear grids. We are able to handle complex topography with slopes of up to 90 degrees. This feature is clarified by a three-dimensional simulation of the flow field around a surface mounted cube ($Re = 7.25 \times 10^6$).

4.2.1 Model set-up

The model set-up is chosen in accordance with a wind-tunnel experiment which was carried out at the Meteorological Institute of Hamburg University. They investigated the flow of a neutrally stratified boundary layer across a wooden cube at a scale of 1:200. This experiment is included in the CEDVAL database (Leitl and Schatzmann 1999).¹ The geometry of the computational domain is shown in Fig. 9, where distances are given as a multiple of the cube height $H = 25$ m. The computational domain covers $15.60 H(x) \times 7.15 H(y) \times 4.22 H(z)$ using $203(x) \times 93(y) \times 50(z)$ grid cells. The centre of the cube is located at a distance of $L = 4.0 H$ downstream of the inflow boundary. This distance is necessary to correctly simulate the upstream influence of the cube. In the x - and y -directions the numerical grid is uniform, while in the z -direction a local refinement of the grid is applied near the lower boundary and near the top of the cube, to improve the resolution of the shear layers. The grid stretching ratio does not exceed a value of 1.12. The lateral boundary conditions are identical to those described in the previous section, using turbulent inflow data at the inlet, zero gradient conditions at the outlet and periodic boundaries in the y -direction (see Fig. 9). The Smagorinsky constant is again set to $C_s = 0.1$.

Turbulent inflow data were, again, generated in a precursor simulation. Slices of the instantaneous velocity fields were stored on disk for 70 nondimensional time units based on the free stream velocity $U_\infty = 4.35 \text{ m s}^{-1}$ and H . The required mean inflow profile and the roughness length $z_0 = 0.08$ m are based on measurements at $x/H = 0$ (without the cube), which are provided in the CEDVAL database.

Since the CEDVAL dataset does not include information about the pressure distribution or periodic fluctuations in the lee, we will also reference the experiment of Hussein and Martinuzzi (1996) who placed the cube in a fully turbulent channel flow and the LES of Krajnovic and Davidson (2001) who used a laminar channel flow as inflow condition. In addition, the experimental results of Castro and Robins (1977), who conducted their investigations in a fully developed boundary-layer flow, will be referenced where appropriate.

4.2.2 Characteristics of the mean flow

The following results have been derived by averaging over the last 556 nondimensional time units of the simulation, which was run in total for 574 nondimensional time units.

The main features of the flow field are schematically depicted in Fig. 5 of Hussein and Martinuzzi (1996). Although this figure was created on the basis of measurements within a turbulent channel flow, many of the detected flow features are known to exist for a wide range of inflow conditions and Reynolds numbers, including the horseshoe vortex, a secondary corner vortex upstream of the cube, a vortex on the roof top, the arch-vortex in the lee, and the secondary corner vortex behind the cube.

¹ www.mi.uni-hamburg.de/CEDVAL-Validation-Data.427.0.html.

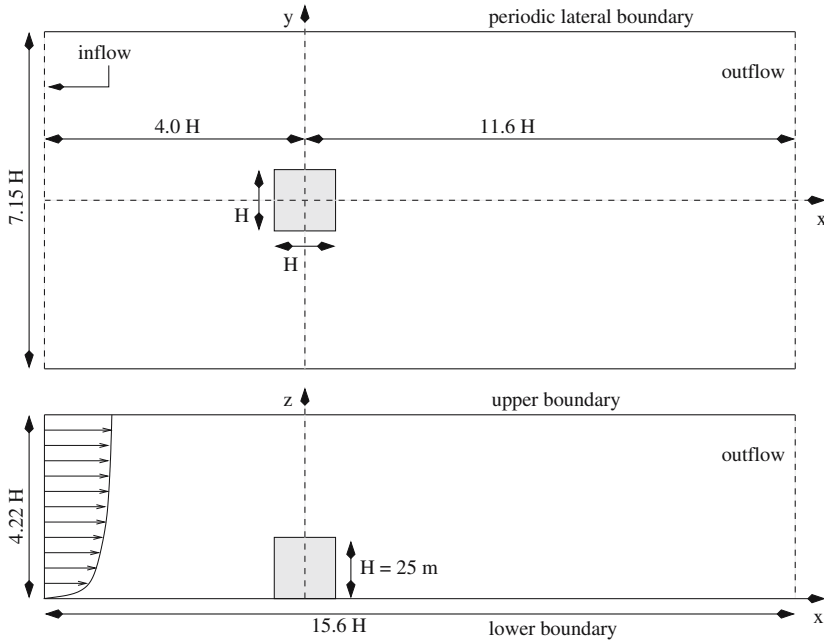


Fig. 9 Geometry of the computational domain for the 3D cube experiment. Distances are given as a multiple of the cube height H

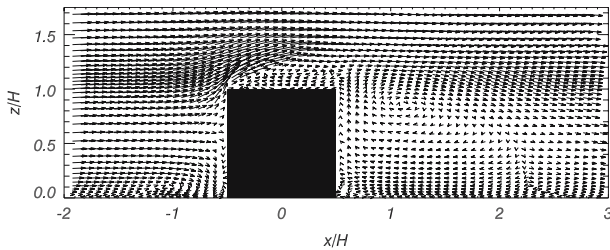


Fig. 10 Time-mean velocity field along the line of symmetry $y/H = 0$

Figure 10 shows the simulated time mean velocity field along the line of symmetry $y/H = 0$. The horseshoe vortex (centred at $x/H = -1.05, z/H = 0.09$) and the arch-vortex (centred at $x/H = 1.1, z/H = 0.84$) are well reproduced. The same holds for the separation at the frontal corner in combination with the backward flow on the roof top. Despite the limitation due to finite resolution, the secondary corner vortices immediately upstream and downstream very close to the cube are visible, although they are not very pronounced.

Table 2 summarises characteristic length scales of the flow field as predicted by the model and derived from the CEDVAL experiment. The results are compared at $x/H = -0.63$ and $z/H = 0.1$ due to the limited resolution of the CEDVAL data. As can be seen, the experimental stagnation point Z_s and separation length X_F in front of the cube are fairly well reproduced. As in the previous simulation, the reattachment length X_R in the lee is slightly overestimated.

Table 2 Characteristic lengths of the flow field around the cube compared to the CEDVAL experiment (stagnation point Z_s at $x/H = -0.63$, separation point X_F and reattachment point X_R at $z/H = 0.1$)

	Z_s/H	X_F/H	X_R/H
CEDVAL	0.64	-0.88	1.50
Model	0.62	-0.96	2.25

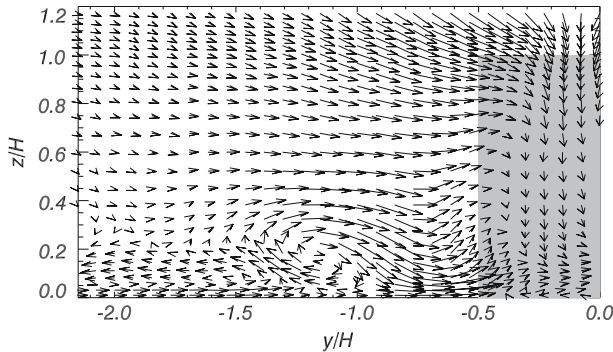


Fig. 11 Time-mean horseshoe vortex in the plane $x/H = 1.25$

In Fig. 11 one leg of the time-averaged horseshoe vortex is shown in the plane $x/H = 1.25$. The simulated position of the vortex core ($y/H \approx -1.15$) is in accordance with the experimental value $y/H = -1.25$ reported by Hussein and Martinuzzi (1996). We found the form of the horseshoe vortex to be highly sensitive to the turbulence intensity upstream of the cube. This feature has already been mentioned by Castro and Robins (1977). We reconduted the same simulation using a constant laminar profile at the inlet and we found the centre of the horseshoe vortex to be located at $y/H \approx -1.7$ for $x/H = 1.25$. This suggests that the legs of the horseshoe vortex move closer to the cube with increasing turbulence intensity upstream. This result is supported by the numerical simulation of Krajnovic and Davidson (2001). The position of the horseshoe vortex they reported for a laminar inflow condition is nearly identical to the position found by us.

Another flow feature that is strongly affected by the intensity of the turbulence upstream of the cube is the shear layer which separates from the leading edge of the roof. Castro and Robins (1977) reported that the upstream turbulence promotes the reattachment of this shear layer. In our simulation the shear layer does not reattach permanently at the roof top (see Fig. 10), although intermittent reattachment does occur. Compared to our laminar inflow condition we also detected the tendency that increased upstream turbulence promotes reattachment of the shear layer. The CEDVAL measurements give no information about the recirculation region above the roof, since the first measuring point (at $z/H = 1.1$) is already outside of the recirculation zone. Thus, the measurements do not indicate whether reattachment occurred at the roof top or not. It can only be stated that the thickness of the recirculation zone is less than $0.1 H$ in the experiment. Our model overpredicts this thickness slightly with a maximum of $0.16 H$ at $x/H = 0.1$.

Figure 12 shows the recirculation vortices behind the cube, which are footprints of the arch-vortex. These two vortices join at the symmetry plane $y/H = 0$ and form the large lee vortex, which has already been mentioned (Fig. 10). The backward flow adjacent to the cube

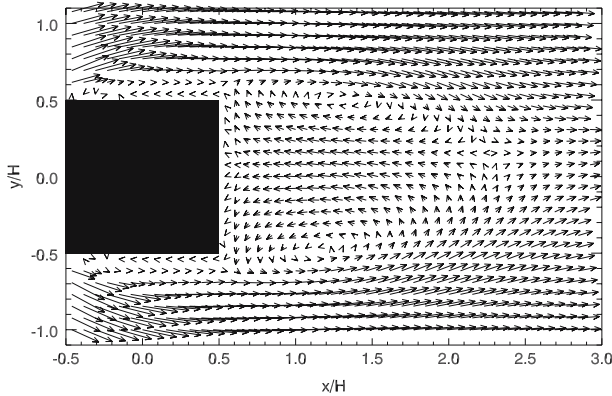


Fig. 12 Time-averaged velocity field in the plane $z/H = 0.15$, showing a cut through the arch-vortex and indicating the vortices along the lateral walls

is due to the lateral vortices. They are not reproduced very well in this simulation. This is possibly due to the fact that no grid refinement was used in the horizontal directions close to the cube. This feature has not been implemented into the model code yet.

4.2.3 The surface pressure field

The mean pressure disturbance on the cube was calculated in terms of the nondimensional pressure coefficient C_p , which is defined as

$$C_p = \frac{p'}{(0.5 \rho_0 U_r^2)}. \tag{27}$$

For U_r , the undisturbed velocity at cube height was chosen. Thus our results can be qualitatively compared to the findings of [Castro and Robins \(1977\)](#).

Figure 13 shows C_p for the different cube walls. A high pressure region is found at the front face where the oncoming flow impinges. The position of the maximum C_p value coincides with the stagnation point Z_S . The leading edges are characterised by strong pressure gradients, leading to suction areas with reverse flow at the roof top and the lateral faces. At the roof top and the lateral walls our results differ somewhat from the results of [Castro and Robins \(1977\)](#). Since our simulation does not show a reattachment of the flow at the roof top, C_p rises at a slower rate behind the leading top edge. The overestimation of C_p at the lateral walls, compared to the results of [Castro and Robins \(1977\)](#), is possibly related to the coarse horizontal resolution. In the lee of the cube we experience a continuous increase of C_p towards the ground. This is due to the backward flow associated with the leeward vortices, which is strongest near the ground. Additionally, in the far wake, the pressure disturbance is markedly higher near the ground than at cube height (not shown). This is associated with the legs of the horseshoe vortex. Those two counter-rotating vortices transport mass downward along the plane of symmetry, which causes the pressure disturbance to rise slightly. This was also observed experimentally by [Hussein and Martinuzzi \(1996\)](#).

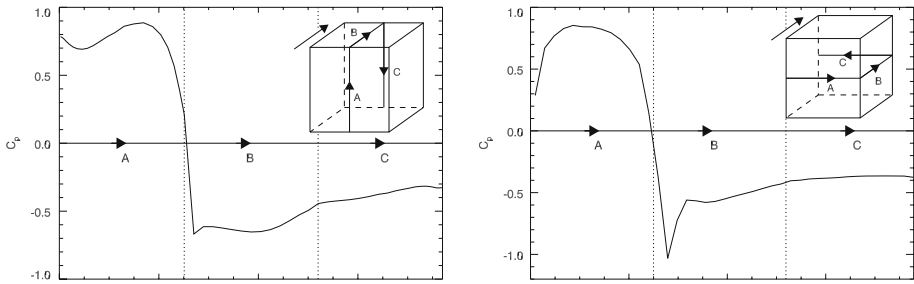


Fig. 13 Surface pressure coefficient C_p on the cube. The picture in the upper right corner shows the displayed path and the direction of the incident flow

4.2.4 Dynamical characteristics and second-order statistics

One of the most pronounced dynamical characteristics of the flow past a surface mounted cube is the periodic vortex shedding in the wake, also known as the Kármán vortex street. Since the Kármán vortices are linked to the spanwise velocity component, we calculated the power spectral density function (PSD) for v , to deduce the dominant frequency. The spectrum was calculated from a time series collected during about 75 vortex shedding cycles in the symmetry plane $y/H = 0$ at the point $x/H = 6, z/H = 0.5$. Figure 14 shows the computed PSD in terms of the Strouhal number

$$Sr = \frac{f H}{U_r}, \tag{28}$$

where U_r is, again, the undisturbed velocity at cube height H and f is the shedding frequency. The $-5/3$ power law is indicated as a dotted line. The spectrum may be divided into three parts; the middle part exhibits the signature of a uniform energy cascade with a slope proportional to $f^{-5/3}$ for about one decade. Thus a significant part of the inertial subrange is explicitly resolved in this simulation. For higher frequencies there is a continuous transition towards a steeper slope. The peak at $Sr = 0.14$, which is the most notable deviation from the $-5/3$ power law is a fingerprint of the quasi periodic vortex shedding in the lee. The Strouhal number found herein agrees well with values reported in the literature (e.g. Hussein and Martinuzzi 1996).

Figures 15 and 16a–d present some turbulence statistics and highlight several important features.

In Fig. 15 a surface plot of the mean turbulent kinetic energy (TKE) in the plane $x/H = 0.75$ is shown. The maxima of TKE are located along the arch-vortex. The secondary maxima to the sides indicate the position of the horseshoe vortex. It should also be noticed, that in the immediate lee the TKE is extremely low. These results are consistent with the measurements of Hussein and Martinuzzi (1996).

Figure 16a–d shows the time mean Reynolds stresses $\langle u'u' \rangle, \langle v'v' \rangle, \langle w'w' \rangle$ and $\langle u'w' \rangle$ along the plane $y/H = 0$, normalised by U_r^2 . The streamwise normal component $\langle u'u' \rangle$ is largest in the vicinity of the horseshoe vortex and along the shear layer separating at the frontal corner. The distributions of $\langle v'v' \rangle$ and $\langle w'w' \rangle$ depict several qualitative similarities. Both stresses show a local maximum at the top of the recirculation region, which is significantly lower compared to $\langle u'u' \rangle$. A second maximum occurs for both near the end of the recirculation region, where the shear layer impinges onto the ground and enhanced mixing occurs. Panel d shows the stress component $\langle u'w' \rangle$. The negative values in the lee

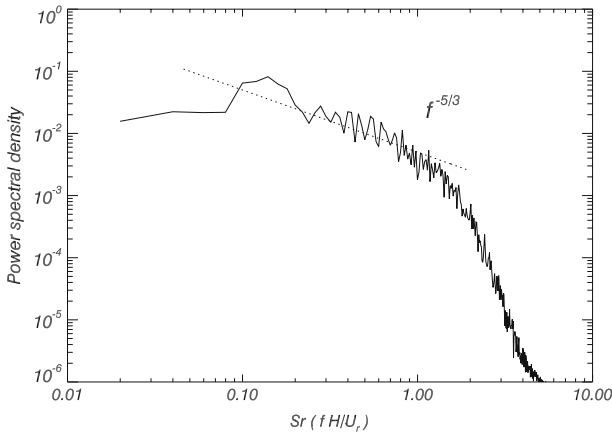


Fig. 14 Power spectral density of spanwise velocity at $x/H = 6$, $y/H = 0$, $z/H = 0.5$

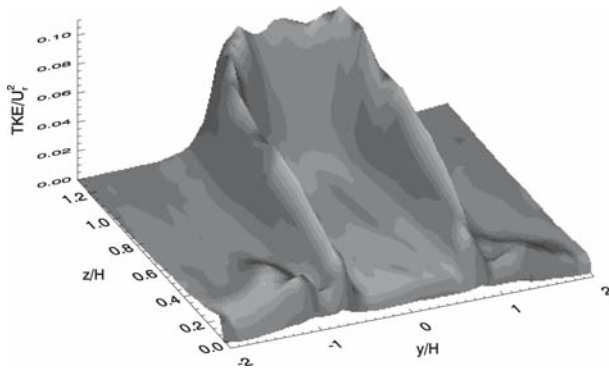


Fig. 15 Surface plot of the mean turbulent kinetic energy (TKE) normalised by U_r^2 along the plane $x/H = 0.75$

of the cube indicate that horizontal momentum is transported downwards. The convergence of this flux in the vicinity of the lower boundary contributes to the acceleration of the horizontal flow in the recovery region. All these features are in qualitative agreement with the experimental results of Hussein and Martinuzzi (1996) and the CEDVAL results.

5 Summary and conclusions

We presented the dry version of a new LES model, which is specifically designed for the simulation of air flow and clouds in the vicinity of highly complex terrain. Specific features of this model are the method of viscous topography for including irregular lower boundaries (Mason and Sykes 1978) and an inflow generation technique proposed by Kataoka and Mizuno (2002). The dynamical model core was validated by reconducting the spreading density current test case developed by Straka et al. (1993). The results are in good agreement with the benchmark solution provided therein.

Simulations were presented for the flow across a quasi 2D ridge and a 3D cube. Non-periodic boundary conditions with fully turbulent inflow data were used. In the case of the

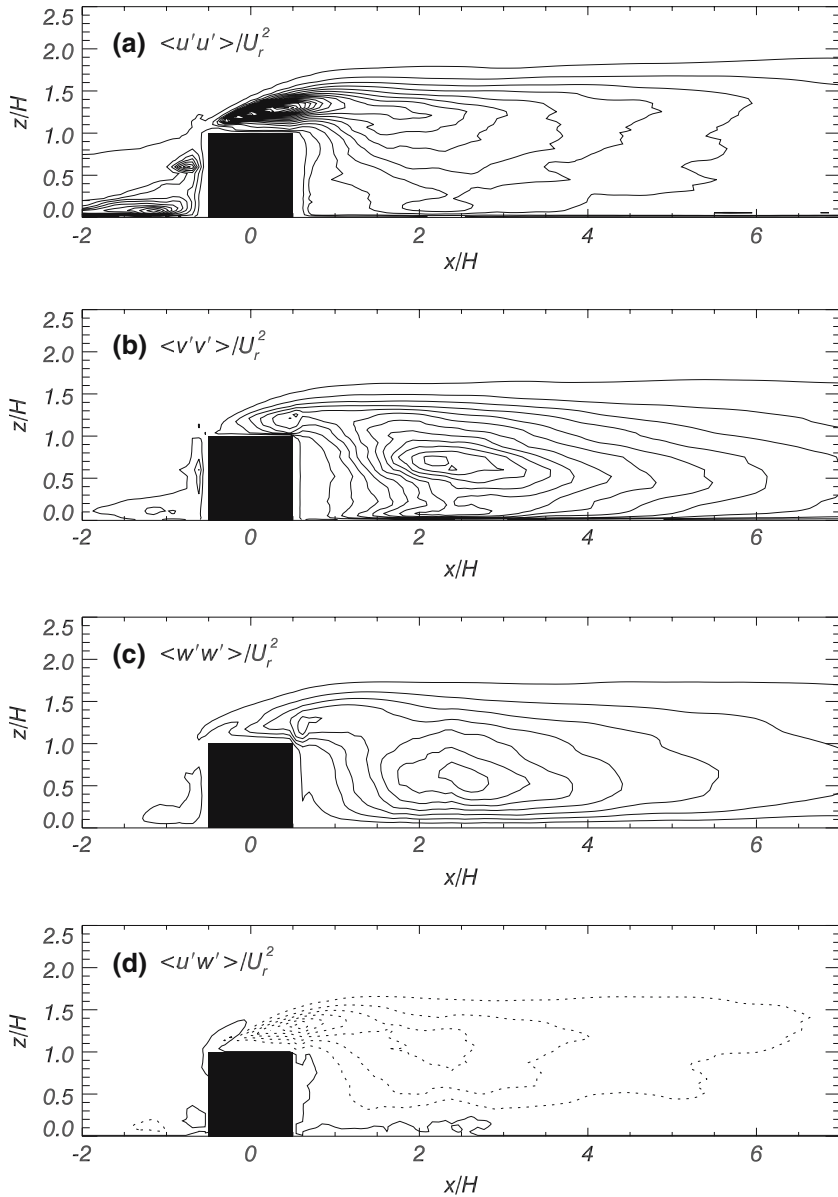


Fig. 16 Contour plots of the time-mean Reynolds stresses along the plane $y/H = 0$. (a) $\langle u'u' \rangle / U_r^2$, (b) $\langle v'v' \rangle / U_r^2$, (c) $\langle w'w' \rangle / U_r^2$, (d) $\langle u'w' \rangle / U_r^2$. Contour intervals of 0.008 are used. Dotted lines indicate negative values

2D ridge the model results were compared against wind-tunnel data (Ishihara et al. 2001). It was shown that, the implemented inflow generation technique and the method of viscous topography perform well. The model results agree with the experimental data except that our model has the tendency to slightly overestimate the length of the leeward separation bubble and the height of the separating shear layer above the ground.

The 3D cube test case showed that our model is able to treat topography with slopes up to 90 degrees and thus has a wider application area compared to most of the models using curvilinear grids. The model results were validated against experimental data from the CEDVAL database (Leitl and Schatzmann 1999) and experiments conducted by Hussein and Martinuzzi (1996) and Castro and Robins (1977). It was shown that, despite the rather coarse horizontal resolution, the model is able to correctly simulate the main flow features in the vicinity of the cube.

Overall we conclude that the method of viscous topography was successfully implemented into a micrometeorological LES model. While this paper focused on the dry model version, part II will present a detailed description of the cloud model and simulations of clouds over complex orography (like e.g. banner clouds).

Acknowledgements Part of this work was funded by the German Research Foundation (DFG) under RE1710/1-2. We thank Prof. T. Ishihara (Univ. of Tokyo), who provided the wind-tunnel data used in this study.

References

- Allen T, Brown AR (2002) Large-eddy simulation of turbulent separated flow over rough hills. *Boundary-Layer Meteorol* 102:177–198
- Cabot W, Moin P (1999) Approximate wall boundary conditions in the large-eddy simulation of high Reynolds number flow. *Flow, Turbulence Comb* 63:269–291
- Castro IP, Robins AG (1977) The flow around a surface-mounted cube in uniform and turbulent streams. *J Fluid Mech* 79(2):307–335
- Clark RA, Ferziger JH, Reynolds WC (1979) Evaluation of subgrid-scale models using an accurately simulated turbulent flow. *J Fluid Mech* 91:1–16
- Deardorff JW (1972) Numerical investigation of neutral and unstable planetary boundary layers. *J Atmos Sci* 29(1):91–115
- Douglas J (1962) Alternating direction methods for three space variables. *Num Math* 4:41–63
- Eichhorn J, Cui K, Flender M, Kandlbinder T, Panhans W-G, Ries R, Siebert J, Trautmann T, Wedi N, Zdankowski WG (1997) A three-dimensional viscous topography mesoscale model. *Contr Atmos Phys* 70(4):301–317
- Froehlich J, Rodi W (2001) Introduction to large eddy simulation of turbulent flows. In: Launder B, Sandham N (eds) *Closure strategies for turbulent and transitional flows*. Cambridge University Press, pp 267–298
- Hussein HJ, Martinuzzi RJ (1996) Energy balance for turbulent flow around a surface mounted cube placed in a channel. *Phys Fluids* 8(3):764–780
- Iizuka S, Kondo H (2006) Large-eddy simulations of turbulent flow over complex terrain using modified static eddy viscosity models. *Atmos Environ* 40:925–935
- Ishihara T, Fujino Y, Hibi K (2001) A wind tunnel study of separated flow over a two-dimensional ridge and a circular hill. *J Wind Eng* 89:573–576. The Fifth Asia-Pacific conference on wind engineering
- Kanda M, Moriawaki R, Kasamatsu F (2004) Large-eddy simulation of turbulent organized structures within and above explicitly resolved cube arrays. *Boundary-Layer Meteorol* 112:343–368
- Kapitza H, Eppel D (1986) A 3-D poisson solver based on conjugate gradients compared to standard iterative methods and its performance on vector computers. *J Comput Phys* 68:474–484
- Kataoka H, Mizuno M (2002) Numerical flow computation around aeroelastic 3D square cylinder using inflow turbulence. *Wind Struct* 5:379–392
- Krajnovic S, Davidson L (2001) Large eddy simulation of the flow around a three-dimensional bluff body. AIAA paper no. 2001-0432, Reno, NV
- Leitl B, Schatzmann M (1999) Generation of high resolution reference data for the validation of micro-scale models. Technical Report Bericht 1443 ISBN 3-18-091443-2, VDI-Kommission Reinhaltung der Luft
- Lilly DK (1962) On the numerical simulation of buoyant convection. *Tellus* 14:148–172
- Lund TS, Wu XW, Squires KD (1998) Generation of turbulent inflow data for spatially-developing boundary layer simulations. *J Comput Phys* 140:233–258
- MacCormack RW (1969) The effect of viscosity in hypervelocity impact cratering. AIAA hypervelocity impact conference, Paper no. 69-354

- Mason PJ (1989) Large-eddy simulation of the convective atmospheric boundary layer. *J Atmos Sci* 46(11):1492–1516
- Mason PJ (1994) Large-eddy simulation: a critical review of the technique quart. *J Roy Meteorol Soc* 120:1–26
- Mason PJ, Sykes RI (1978) A simple cartesian model of boundary layer flow over topography. *J Comput Phys* 28:198–210
- Mason PJ, Thomson DJ (1992) Stochastic backscatter in large-eddy simulations of boundary layers. *J Fluid Mech* 242:51–78
- Mendez-Nunez LR, Caroll JR (1993) Comparison of Leapfrog, Smolarkiewicz and MacCormack schemes applied to nonlinear equations. *Mon Wea Rev* 121:565–578
- Moin P, Kim J (1982) Numerical investigation of turbulent channel flow. *J Fluid Mech* 118:341–377
- Neumann J, Wengle H (2003) DNS and LES of passively controlled turbulent backward-facing step flows. *Flow, Turb Comb* 71:297–310
- Orlanski I (1976) A simple boundary condition for unbounded hyperbolic flows. *J Comput Phys* 21:251–269
- Patrnos A, Kistler AL (1977) A numerical study of the Chicago Lake Breeze. *Boundary-Layer Meteorol* 12:93–123
- Smolarkiewicz PK, Clark TL (1986) The multidimensional positive definite advection transport algorithm: further developments and applications. *J Comput Phys* 67:396–438
- Smolarkiewicz PK, Grabowski WW (1990) The multidimensional positive definite advection transport algorithm: nonoscillatory option. *J Comput Phys* 86:355–375
- Straka JM, Wilhelmson RB, Droegemeier KK (1993) Numerical solutions of a non-linear density current: a benchmark solution and comparisons. *Int J Num Meth Fluids* 17:1–22